Observation of Transient Structural-Transformation Dynamics in a Cu_2S Nanorod

Haimei Zheng *et al.*

Science **333**, 206 (2011);
DOI: 10.1126/science.1204713

This copy is for your personal, non-commercial use only.

If you wish to distribute this article to others, you can order high-quality copies for your colleagues, clients, or customers by clicking here.

Permission to republish or repurpose articles or portions of articles can be obtained by following the guidelines here.

The following resources related to this article are available online at www.sciencemag.org (this information is current as of October 24, 2014):

Updated information and services, including high-resolution figures, can be found in the online version of this article at:
http://www.sciencemag.org/content/333/6039/206.full.html

Supporting Online Material can be found at:
http://www.sciencemag.org/content/suppl/2011/07/06/333.6039.206.DC1.html

This article **cites 29 articles**, 6 of which can be accessed free:
http://www.sciencemag.org/content/333/6039/206.full.html#ref-list-1

This article has been **cited by** 1 articles hosted by HighWire Press; see:
http://www.sciencemag.org/content/333/6039/206.full.html#related-urls

This article appears in the following **subject collections:**
Materials Science
http://www.sciencemag.org/cgi/collection/mat_sci

Downloaded from www.sciencemag.org on October 24, 2014

Science (print ISSN 0036-8075; online ISSN 1095-9203) is published weekly, except the last week in December, by the American Association for the Advancement of Science, 1200 New York Avenue NW, Washington, DC 20005. Copyright 2011 by the American Association for the Advancement of Science; all rights reserved. The title *Science* is a registered trademark of AAAS.

38. E. Waxman, *Astrophys. J. Lett.* **452**, L1 (1995).
39. N. Vlahakis, A. Königl, *Astrophys. J.* **605**, 656 (2004).
40. H. C. Spruit, D. A. Uzdensky, *Astrophys. J.* **629**, 960 (2005).
41. The uncertain relative contributions of the host galaxy and the optical/IR transient result in very large uncertainties for the *J* and *z* photometric data points. In this model, the radio and IR emission are produced by synchrotron radiation from an extended source, whereas the x-ray emission is dominated by the Compton scattering of external photons from the accretion disk (for illustrative purposes, we assume a 10^6 $M_\odot$ MBH). As in the orange model, the x-ray emission is dominated by external Compton scattering, whereas the peak at high energies results from synchrotron self-Compton emission. An additional synchrotron component from a mildly relativistic blast-wave afterglow at larger radius is invoked to explain the bright radio and millimeter fluxes.
42. S. Campana, L. Foschini, G. Tagliaferri, G. Ghisellini, S. Covino, "GRB 110328/Swift J164449.3+573451: Fermi observations" (GCN Circular 11851, NASA Goddard Space Flight Center, Greenbelt, MD, 2011).
43. Although we have modeled the "quiescent" SED, a similar external Compton model can be made to fit the "flaring" x-ray state, provided that the jet luminosity is accordingly increased.
44. H. Krawczynski *et al.*, *Astrophys. J.* **601**, 151 (2004).
45. For the models, $\Gamma_j = 10$ and the magnetic field strength $B = 10$ (0.001) Gauss for the synchrotron + external Compton + afterglow (synchrotron + external Compton + self-Compton) model. In the synchrotron + external Compton + afterglow model, we find a disk luminosity of $L_{\rm disk} = 0.4\ L_{\rm Edd}$, with $L_{\rm Edd} = 1.3 \times 10^{44}$ erg s^{-1}, corresponding to a BH with 10^6 $M_\odot$. In the synchrotron + external Compton + self-Compton model, we find a disk luminosity of $L_{\rm disk} = 0.04\ L_{\rm Edd}$, with $L_{\rm Edd} = 1.3 \times 10^{45}$ erg s^{-1}, corresponding to a BH with 10^7 $M_\odot$.

Acknowledgments: We thank R. Romani, C. McKee, L. Blitz, and J. Hjorth for close reads of drafts of this work and for helpful interactions. We are grateful to the entire Swift team for work on their remarkable observatory that enabled discovery of this event. Swift, launched in November 2004, is a NASA mission in partnership with the Italian Space Agency and the UK Space Agency. Swift is managed by NASA Goddard. Pennsylvania State University controls science and flight operations from the Mission Operations Center in University Park, PA. Los Alamos National Laboratory provides gamma-ray imaging analysis. J.S.B. and his group were partially supported by grants NASA/NNX10AF93G, NASA/NNX10AI28G, and NSG/AST-100991. D.G. acknowledges support from the Lyman Spitzer Jr. Fellowship awarded by the Department of Astrophysical Sciences at Princeton University. B.D.M. is a NASA Einstein Fellow and is supported by NASA through Einstein Postdoctoral Fellowship grant number PF9-00065 awarded by the Chandra X-ray Center, which is operated by the Smithsonian Astrophysical Observatory for NASA under contract NAS8-03060. S.B.C. acknowledges generous support from Gary and Cynthia Bengier, the Richard & Rhoda Goldman fund, NASA/Swift grant NNX10AI21G, NASA Fermi grant NNX10A057G, and NSF grant AST-0908886. N.R.B. is a NASA Einstein Fellow. W.H.L. is supported in part by Consejo Nacional de Ciencia y Tecnología grant 83254. A.J.vdH. was supported by NASA grant NNH07ZDA001-GLAST. The primary references for the data presented here were given in the text and may be found in (*20*) or in the NASA/Swift archive (http://heasarc.nasa.gov/docs/swift/archive/).

Supporting Online Material

www.sciencemag.org/cgi/content/full/science.1207150/DC1
Materials and Methods
Figs. S1 to S3
References

18 April 2011; accepted 6 June 2011

10.1126/science.1207150

Observation of Transient Structural-Transformation Dynamics in a Cu_2S Nanorod

Haimei Zheng,[1]* Jessy B. Rivest,[2] Timothy A. Miller,[3] Bryce Sadtler,[1,4]† Aaron Lindenberg,[3] Michael F. Toney,[5] Lin-Wang Wang,[1] Christian Kisielowski,[1,6] A. Paul Alivisatos[1,4]*

The study of first-order structural transformations has been of great interest to scientists in many disciplines. Expectations from phase-transition theory are that the system fluctuates between two equilibrium structures near the transition point and that the region of transition broadens in small crystals. We report the direct observation of structural fluctuations within a single nanocrystal using transmission electron microscopy. We observed trajectories of structural transformations in individual nanocrystals with atomic resolution, which reveal details of the fluctuation dynamics, including nucleation, phase propagation, and pinning of structural domains by defects. Such observations provide crucial insight for the understanding of microscopic pathways of phase transitions.

First-order structural transformations in solids play an important role in a variety of processes ranging from information storage (*1*, *2*) to materials processing (*3*). An understanding of the microscopic mechanisms of structural transformations is critical for understanding and controlling these processes. In nanoscale systems, the energetic barrier to a structural transformation scales with crystal size. When the size of a nanocrystal is in a regime where thermal energy is comparable to the energy barrier for phase transformation, fluctuations between two stable structures occur at the transition point (*4*, *5*). This is relevant to many molecular and solid-state phenomena near equilibrium, and there have been numerous studies of the ensemble fluctuations that accompany these phase transformations (*6*–*10*). However, in ensemble studies, only the average characteristics of the fluctuations can be observed, and many important features may be completely obscured by parallel, unsynchronized transition processes. In this study, we focus on observing the individual structural fluctuations in a single nanocrystal by taking advantage of recent advances in transmission electron microscopy (TEM). Advances in electron optics and recording systems for TEM have enabled rapid imaging with single-atom sensitivity across the periodic table and with greater collection efficiency (*11*–*13*). This provides extraordinary opportunities to study the structural-transformation dynamics in situ with atomic resolution.

A model system chosen for this study is the structural transformation between the low- and high-chalcocite phases of copper sulfide (Cu_2S) nanorods (i.e., with dimensions of 5 by 28 nm). We synthesize Cu_2S nanorods through a colloidal solution process, and the nanorods show the low-chalcocite phase at room temperature (*14*). The low-chalcocite is monoclinic with a space group of $P2_1/c$ or Pc, in which copper atoms partially occupy the lattice sites within a distorted hexagonal sulfur lattice frame (*15*). When Cu_2S transforms into the high-chalcocite structure (a space group of $P6_3/mmc$), the hexagonal sulfur sublattice remains rigid, but copper atoms occupy different lattice sites (*16*, *17*) (see the Cu-S phase diagram in fig. S1). In Cu_2S nanorods, the structural transformation is poised relatively close to room temperature [376 K in bulk and ~337 ± 4 K in the nanorods (*18*)]; therefore, thermal energy sufficient to induce the structural transformation is low enough to avoid melting, ripening, defect rearrangement, or other unwanted perturbations of the nanocrystals. The nanorod geometry allows for the atomic structure of the material to be resolved through the thickness of a few nanometers, whereas the ability to independently control the length enables us to adjust the number of fluctuating domains within the particle.

Another convenient feature of the Cu_2S nanorod system is that because the transformation temperature is relatively low, heating from the electron beam can be used to induce the structural transformations. Samples for this investigation are prepared by drop-casting a dilute solution of Cu_2S nanorods on a conductive carbon grid. While imaging by TEM, part of the energy dissipated from the interaction between the nanocrystal and the

---

[1]Materials Sciences Division, Lawrence Berkeley National Laboratory, Berkeley, CA 94720, USA. [2]Department of Mechanical Engineering, University of California, Berkeley, CA 94720, USA. [3]Department of Materials Science and Engineering, Photon Science, Stanford University, Stanford, CA 94305, USA. [4]Department of Chemistry, University of California, Berkeley, CA 94720, USA. [5]Stanford Synchrotron Radiation Laboratory, Palo Alto, California, 94025, USA. [6]National Center for Electron Microcopy, Lawrence Berkeley National Laboratory, Berkeley, CA 94720, USA.

*To whom correspondence should be addressed. E-mail: hmzheng@lbl.gov (H.M.); alivis@berkeley.edu (A.P.A.)

†Present address: Division of Chemistry and Chemical Engineering, California Institute of Technology, Pasadena, CA 91125, USA.

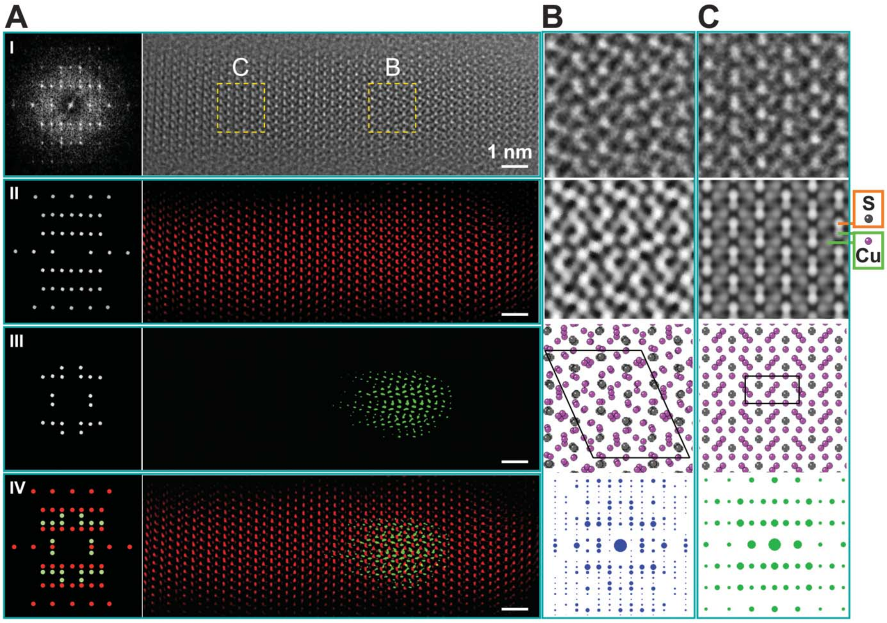

Fig. 1. Images and image process to visualize the low- and high-chalcocite structures in a Cu_2S nanorod. (**A**) Image process to highlight the low-chalcocite (green) and high-chalcocite (red) domains in HRTEM images of a Cu_2S nanorod. (I) Obtain the fast Fourier transform (FFT) pattern (left) of the original HRTEM image (right). (II) Place a mask in the FFT pattern in (I) allowing the diffraction spots of the hexagonal lattice to pass (left). The corresponding filtered image shows the high-chalcocite domain or the hexagonal lattice frame of low-chalcocite (right). (III) Place a mask in the FFT pattern (I) only allowing the low-chalcocite diffraction spots to pass (left). The corresponding filtered image shows the low-chalcocite domain (right). (IV) Highlight the two structures in the Cu_2S nanorod by overlapping the two filtered images (right) and the two masks in II and III (left). (**B**) The low-chalcocite structure in the [110] zone axis. Images from top to bottom: the atomic structure from the selected section in (A) (top), simulated image (second row), structural model (third row), and simulated electron diffraction (bottom). In the atomic structure in the top image, the low-chalcocite (in the core) is superimposed with the high-chalcocite structure (outer layer of the nanorod). (**C**) The high-chalcocite structure in the [010] zone axis displayed in the same order as in (B).

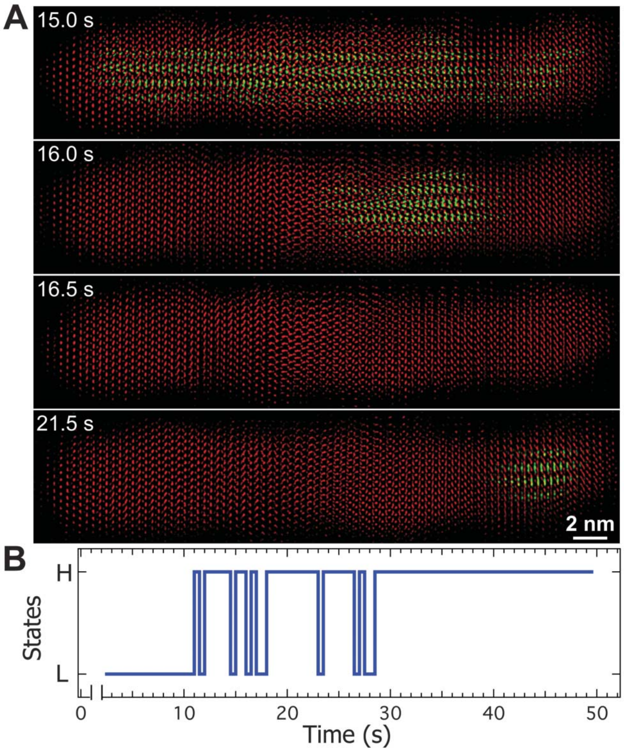

Fig. 2. Trajectory of the structural transformations in a Cu_2S nanorod. (**A**) Sequential images showing the low-chalcocite structure (green), mixed structure (mixed green and red domains), and the pure high-chalcocite structure (red). (**B**) Trajectory of structural transformations from a low-chalcocite structure (L) to the transition period with fluctuations between the two phases, and the final stable high-chalcocite structure (H).

electron beam (e.g., inelastic scattering of the incident electrons) is converted into heat. The equilibrium temperature of the nanocrystal is determined by the electron current density (energy input) and thermal dissipation. There have been many reports on the heating of a sample by electron-beam irradiation, where a wide range of temperature increases have been reported (*19*–*21*). Here, we found that under controlled electron-beam irradiation a Cu_2S nanorod on a carbon thin film can be heated above its phase-transition temperature of 337 ± 4 K [i.e., it is estimated that at steady-state conditions, a Cu_2S nanorod is heated to ~347.8 K under electron-beam irradiation with a current density of 5000 electrons per Å^2 per second; see details in the supporting online material (*18*)]. The structural-transformation temperature of an ensemble of Cu_2S nanorods without electron-beam irradiation was verified by x-ray diffraction studies of a powder of Cu_2S nanorods (*18*).

We have estimated that fluctuations between the two structures in the Cu_2S nanorods should be observable under the above imaging conditions. As the system approaches the critical temperature, the relative probability of observing the two phases is given by (*22*)

$$P_1/P_2 = \exp\left[\frac{-(E_1 - E_2)\Delta T}{T_C k_B T}\right] \qquad (1)$$

where P_1 is the probability of observing phase 1, P_2 is the probability of observing phase 2, T is temperature, T_c is the phase transition temperature, k_B is the Boltzmann constant, $E_1 - E_2 = (\varepsilon_1 - \varepsilon_2)N$ is the latent heat (enthalpy of transition), $(\varepsilon_1 - \varepsilon_2)$ is the transition enthalpy per Cu_2S unit cell, and N is the number of Cu_2S unit cells. For a Cu_2S nanocrystal of a given size (for instance, $N = 1000$), if we take $\Delta\varepsilon$ = 3849 J/mol (40 meV per unit cell) (*23*), $T_c = 337 \pm 4$ K, and $P_1/P_2 = e^{-1}$ (at the critical phase-transition temperature, the thermal fluctuation of kT is equal to the transition energy), we find that $\Delta T \sim 0.2$ K. This suggests that the structural transformation in a Cu_2S nanocrystal with N = 1000 (2- to 4-nm domains) occurs within a temperature range of $T_c \pm 0.2$ K. Our experiments show that this broadening in the transition temperature provides ample opportunity to collect structural-transformation trajectories.

Figure 1 illustrates the image-processing technique that we have developed to visualize the different structural domains within a Cu_2S nanorod in a high-resolution TEM (HRTEM) image. We apply digital masks in Fourier space, which are characteristic of each of the two phases. The corresponding filtered real-space images allow for the identification of the low- or high-chalcocite domains in a single nanocrystal. For noise reduction, our mask design captures only Fourier components above a given threshold [e.g., signal/noise > 10; see II and III in Fig. 1A, in which the MacTempas image simulation program (*24*) was used for image processing and Adobe Photoshop software was used for false coloring of the images (see fig. S2)]. As a result, the filtered images do not represent all atom positions in the two phases, but rather reflect the size and shape of the structural domains. By applying this procedure to a time series of HRTEM images, the spatial distribution of the two phases within a single Cu_2S nanorod can be tracked in time.

We recorded a series of HRTEM images continuously at a rate of 0.5 s per frame using an aberration-corrected transmission electron microscope operated at 80 kV. The microscope is tuned to a spherical aberration (Cs) value of –0.015 mm, and the defocus is set to ~8 nm. Under these conditions, atomic columns appear bright and the intensities reveal the positions of copper and sulfur as long as the surface roughness of the sample does not substantially exceed the focal spread in the beam direction (~1 nm) (*13*). Thus, the atomic structures of the two phases are resolved in a single image (Fig. 1, B and C; a comparison between the single image and the phase image by exit-wave reconstruction for each phase is shown in fig. S3). By applying the above image processing to the HRTEM image series collected under these conditions, the dynamic spatial distribution of the structural domains, as well as changes in the atomic structure of a Cu_2S nanorod during structural transformation, can be observed.

Figure 2 shows the trajectory of the structural transformation from low- to high-chalcocite phase in a single Cu_2S nanorod (similar trajectories of phase transitions have been observed in many other Cu_2S nanorods). The nanorod initially has the expected low-chalcocite structure. Under electron-beam irradiation, either the complete Cu_2S nanorod or a portion of it temporarily transforms into high-chalcocite phase, and the two structures fluctuate for an extended period of time. Ultimately, the nanorod transforms into the stable high-chalcocite phase (Fig. 2; see details in movie S1). In Fig. 2B, "H" represents the states with a pure high-chalcocite structure in the Cu_2S nanorod, and "L" represents the presence of low-chalcocite phase in the nanorod, including both the pure low-chalcocite structure and a mixed structure. By decreasing (or increasing) the electron current density, the duration of the period during which fluctuations are observed increases (or decreases, respectively). We have further noticed that once the Cu_2S nanorod has transformed into the stable high-chalcocite structure, the structure remains, even when the electron beam is shut off for a period of time. This suggests that the high-chalcocite structure tends to be trapped in the nanorod (*25*).

The high level of detail of our observations provides insight into the nature of structural transformation in a Cu_2S nanorod. For instance, we can see differences in the nucleation processes between the forward and reverse transformations. At the onset of the transition from low- to high-chalcocite, the high-chalcocite structure is observed at the outer surface of the low-chalcocite nanorod (Fig. 3A). The high-chalcocite propagates inward concentrically until the whole nanorod is transformed into pure high-chalcocite phase. This transition behavior is similar to a solid-liquid phase transition, such as the high-temperature melting of a metal nanoparticle (*26*). When the low-chalcocite phase reappears (nucleates), it is located at the core of the high-chalcocite Cu_2S nanorod (Figs. 2 and 3, also see movies S1, S3, and S5). The low-chalcocite domain (i.e., 2 to 4 nm in diameter) can propagate along the long-axis of the nanorod or grow into a larger domain, which suggests that the transition from high- to low-chalcocite is a nucleation and growth process. It is likely that there are rapid structural fluctuations of even smaller domains during the nucleation process.

The dynamics of the Cu_2S structural transformation are strongly affected by the presence of defects. Defects, such as a stacking fault across a Cu_2S nanorod, separate the nanorod into different structural domains (Fig. 4 A and B). Trajectories of structural fluctuations are different in adjacent domains (Fig. 4C; also see movie S3). The smaller domain (zone II) fluctuates more frequently than a larger domain (zone I). We have observed the prevalence of high-chalcocite structure at the domain boundary during the transition, which is probably due to the higher energy of the defect sites. One can imagine that complex phase-transition kinetics occurs in bulk materials and nanocrystal ensembles due to parallel phase-transition processes in different parts of the sample. The nanorods present a simplified case where fluctuations in just a few domains along the length of the nanorod can be monitored.

We have estimated the fluctuation kinetics by using a thermodynamic fluctuation model (*27*). For a small system embedded in a larger reservoir (e.g., a low-chalcocite domain at the core of a high-chalcocite nanorod), the probability for the small system to have an internal energy of E is

$$P(E) = \exp\left[\frac{-(E - E_0)^2}{2k_B T^2 C}\right] \qquad (2)$$

where E_0 is the average internal energy of the small system and C is the specific heat for the small system (*27*). We assume that the structural transformation occurs when the energy change $(E - E_0)$ is equal to the interface energy (E_s) of the small system. The fluctuation time τ can be expressed as

$$\tau = \tau_0 \exp\left[\frac{E_s^2}{2k_B T^2 C}\right] \qquad (3)$$

Here, τ_0 is an attempt time for the atoms to execute the transition, usually taken as a vibra-

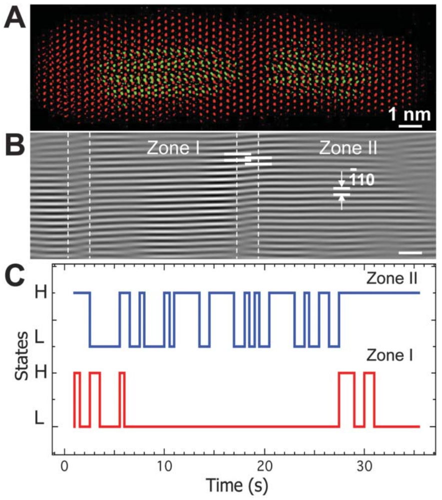

Fig. 4. The effect of defects on the structural transformations of a Cu_2S nanorod. (**A**) HRTEM image after image processing highlighting the low-chalcocite domains (green). (**B**) Filtered image showing ($\bar{1}10$) planes, where the regions marked with dashed lines highlight two stacking faults. (**C**) Trajectories of structural fluctuations in zones I and II during the transition period.

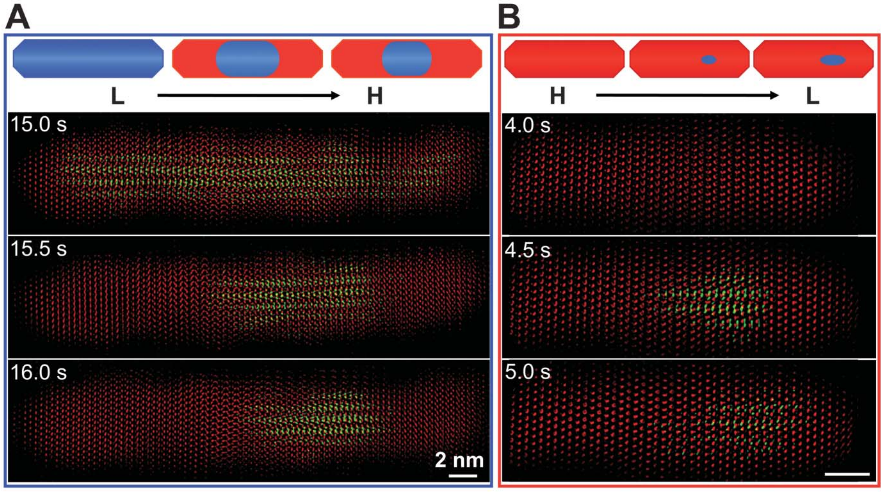

Fig. 3. Sequential images showing the pathways of structural transformations in two Cu_2S nanorods. (**A**) The high-chalcocite structure (red) is formed at the outer surface of the nanorod. The low-chalcocite domain is shown in green. (**B**) The low-chalcocite structure nucleates at the core of the high chalcocite.

tional period, which is on the order of picoseconds. E_s between high- and low-chalcocite phases results from the different Cu arrangements in these two phases and the related extra Ewald energy at the interface. This is similar to the case of the interface between wurtzite (WZ) and zincblende (ZB), where the different second nearest-neighbor atomic positions cause different Ewald energies in these two phases. It has been found that the interface energy between WZ and ZB per surface unit cell is similar to the energy difference per unit cell (*28*). Thus, if we take this approximation that the interface energy between low- and high-chalcocite is the same as the internal energy difference between these two phases, $(\varepsilon_1 - \varepsilon_2) = 40$ meV per unit cell (*23*), and assume that there are N Cu_2S unit formulae inside a spherical core, we have $E_s = (36\pi)^{1/3}N^{2/3}(\varepsilon_1 - \varepsilon_2)$. Note that $C = C_{unit}N$, and $C_{unit} = 52$ J/mol·K (*23*). Thus, from Eq. 3, we get $\tau \sim 2$ s when $N = 1000$ and $\tau_0 = 1$ ps (*29*). This fluctuation time is of the same order as our observed experimental value.

In summary, we have observed dynamic structural transformations of a single Cu_2S nanorod from a low- to a high-chalcocite structure. The influence of the surface and interface energies on nucleation and pinning phenomena of a particular phase by defects suggests strategies for stabilizing metastable structures. The ability to directly visualize these processes will aid in the future design of materials with new and controlled phases.

References and Notes

1. M. H. R. Lankhorst, B. W. S. M. M. Ketelaars, R. A. M. Wolters, *Nat. Mater.* **4**, 347 (2005).
2. S. H. Lee, Y. Jung, R. Agarwal, *Nat. Nanotechnol.* **2**, 626 (2007).
3. J. Christian, *The Theory of Transformations in Metals and Alloys* (Pergamon, London, 1965).
4. H. E. Stanley, *Introduction to Phase Transitions and Critical Phenomena* (Oxford Univ. Press, New York, 1987).
5. M. S. S. Challa, D. P. Landau, K. Binder, *Phase Transit.* **24**, 343 (1990).
6. K. Jacobs, D. Zaziski, E. C. Scher, A. B. Herhold, A. Paul Alivisatos, *Science* **293**, 1803 (2001).
7. Q. X. Guo *et al.*, *Nano Lett.* **8**, 972 (2008).
8. R. F. Smith *et al.*, *Phys. Rev. Lett.* **101**, 065701 (2008).
9. J. S. Wittenberg, M. G. Merkle, A. P. Alivisatos, *Phys. Rev. Lett.* **103**, 125701 (2009).
10. Z. W. Wang *et al.*, *Proc. Natl. Acad. Sci. U.S.A.* **107**, 17119 (2010).
11. M. Lentzen, *Microsc. Microanal.* **14**, 16 (2008).
12. C. Ö. Girit *et al.*, *Science* **323**, 1705 (2009).
13. R. Erni *et al.*, *Phys. Rev. B* **82**, 165443 (2010).
14. B. Sadtler *et al.*, *J. Am. Chem. Soc.* **131**, 5285 (2009).
15. H. T. Evans, *Nat. Phys. Sci.* **232**, 69 (1971).
16. M. J. Buerger, B. J. Wuensch, *Science* **141**, 276 (1963).
17. A. Putnis, *Am. Mineral.* **62**, 107 (1977).
18. Supporting material is available on *Science* Online.
19. T. Yokota, M. Murayama, J. M. Howe, *Phys. Rev. Lett.* **91**, 265504 (2003).
20. R. F. Egerton, P. Li, M. Malac, *Micron* **35**, 399 (2004).
21. A. Reguer *et al.*, *Ultramicroscopy* **110**, 61 (2009).
22. M. S. S. Challa, D. P. Landau, K. Binder, *Phys. Rev. B* **34**, 1841 (1986).
23. D. J. Chakrabarti, D. E. Laughlin, *J. Phase Equil.* **4**, 254 (1983).
24. www.totalresolution.com
25. R. W. Potter, *Econ. Geol.* **72**, 1524 (1977).
26. S. L. Lai, J. Y. Guo, V. Petrova V, G. Ramanath, L. H. Allen, *Phys. Rev. Lett.* **77**, 99 (1996).
27. L. D. Landau, E. M. Lifshitz, *Statistical Physics* (Pergamon, New York, 1980).
28. F. Glas, *J. Appl. Phys.* **104**, 093520 (2008).
29. A. F. Voter, *Phys. Rev. B* **34**, 6819 (1986).

Acknowledgments: We thank U. Dahmen at National Center for Electron Microscopy (NCEM) and E. Borrero and C. Dellago at University of Vienna for helpful discussions. The authors are grateful to the support of Helios Solar Energy Research Center (SERC) and NCEM, which are funded by the director of the Office of Science, Office of Basic Energy Sciences (BES), Materials Science and Engineering Division of the U.S. Department of Energy (DOE) under contract no. DE-AC02-05CH11231. TEM experiments were performed using TEAM0.5 microscope at NCEM. X-ray experiments were performed at the Stanford Synchrotron Radiation Laboratory, a DOE-BES user facility. J.B.R. was funded by a fellowship from Intel Corporation, and T.A.M. and A.L. were supported by the DOE BES Materials Sciences and Engineering Division. H.Z. conceived the work and performed the experiments; H.Z. and A.P.A. analyzed the data and wrote the paper; J.B.R. prepared nanorod samples, took ensemble x-ray data, and edited the paper; B.S. contributed to nanorod sample preparation and edited the paper; M.F.T., A.L., and T.A.M. provided x-ray analysis infrastructure; L.-W.W. provided theoretical calculation and edited the paper; and C.K. contributed to image analysis and edited the paper.

Supporting Online Material

www.sciencemag.org/cgi/content/full/333/6039/206/DC1
Materials and Methods
SOM Text
Figs. S1 to S4
Table S1
References (*30–35*)
Movies S1 to S6

23 February 2011; accepted 25 May 2011
10.1126/science.1204713

Palladium-Catalyzed Aerobic Dehydrogenation of Substituted Cyclohexanones to Phenols

Yusuke Izawa, Doris Pun, Shannon S. Stahl*

Aromatic molecules are key constituents of many pharmaceuticals, electronic materials, and commodity plastics. The utility of these molecules directly reflects the identity and pattern of substituents on the aromatic ring. Here, we report a palladium(II) catalyst system, incorporating an unconventional *ortho*-dimethylaminopyridine ligand, for the conversion of substituted cyclohexanones to the corresponding phenols. The reaction proceeds via successive dehydrogenation of two saturated carbon-carbon bonds of the six-membered ring and uses molecular oxygen as the hydrogen acceptor. This reactivity demonstrates a versatile and efficient strategy for the synthesis of substituted aromatic molecules with fundamentally different selectivity constraints from the numerous known synthetic methods that rely on substitution of a preexisting aromatic ring.

Phenols are common precursors and core structures of industrial chemicals ranging from pharmaceuticals to polymers. The introduction of chemical functional groups with specific patterns around the aromatic ring represents a key challenge in the preparation of these molecules (*1*). Electrophilic aromatic substitutions are classical chemical reactions that remain among the most versatile methods for the synthesis of substituted phenols; however, strong electronic directing effects associated with these reactions limit their utility to the preparation of ortho- and para-substituted derivatives. This limitation has inspired extensive efforts to identify complementary routes to substituted phenols, such as a recent two-step arene C–H borylation/oxidation procedure for the introduction of a hydroxyl group into an aromatic ring, guided by steric rather than electronic effects (*2*). Recent advances in palladium-catalyzed aerobic oxidation reactions (*3–5*) suggested to us that diverse phenol derivatives, including those with meta substitution, could be accessed by dehydrogenation of cyclohexanones via sequential Pd-mediated C–H activation/β-hydride elimination steps, followed by tautomerization of the resulting dienone product (Fig. 1A). This strategy is appealing because Pd^{II}–hydride intermediates formed in this mechanism could be oxidized by molecular oxygen (*6*, *7*), thereby enabling the overall process to be catalytic in Pd with water as the sole by-product (Fig. 1B). Successful catalysts for this class of reactions could find broad utility owing to the numerous straightforward chemical reactions that provide access to substituted cyclohexanones, including enolate arylation and alkylation methods, conjugate addition to cyclohexenones, and Robinson annulation and Diels-Alder reactions (Fig. 1C).

The preparation of phenols from ketone precursors have been explored previously (*8–16*). Condensation reactions of acyclic ketones, for example, with β-ketoaldehydes or β-diketones, enable direct access to substituted phenols (*8*), but low product yields, limited access to starting materials, and/or formation of isomeric products

---

Department of Chemistry, University of Wisconsin–Madison, 1101 University Avenue, Madison, WI 53706, USA.

*To whom correspondence should be addressed. E-mail: stahl@chem.wisc.edu